An Adaptive Robust Enhanced Time-Delay Impedance Controller for a Cell Puncture Device With Soft Contact Environment

Zhicheng Song, Yang Wu, Yaoyao Wang, *Member, IEEE*, Jie Ling, *Member, IEEE*, and Yangwei Wang

***Abstract*—This paper proposes a novel adaptive robust enhanced time-delay impedance controller (ARETDIC) based on the Hunt–Crossley (HC) model. The proposed ARETDIC is used to precisely control force/position for cell puncture devices operating within a soft interaction environment. Firstly, the impedance model is formulated utilizing the HC model, followed by a comprehensive discussion of its steady-state performance. To attain the target impedance, a new integral terminal sliding mode manifold is proposed by constructing an intermediate variable. Subsequently, the traditional time-delay control framework is enhanced by compensating for the well-known time-delay error using time-delay information from the previous time step. Furthermore, a new adaptive robust term is introduced to ensure the system's robustness against lumped disturbances. The stability of the proposed ARETDIC is proven using the Lyapunov theory. Finally, the superiority and effectiveness of the proposed ARETDIC are verified by experiments. The results indicate that the proposed ARETDIC achieves the best control performance compared to the other three benchmark controllers, successfully completing the cell puncture task.**

***Note to Practitioners*—This paper was motivated by the challenge of achieving precise force and position control in cell puncture devices operating within soft contact environments. This paper suggests a new controller using time-delay control (TDC) to eliminate the need for a detailed system dynamics model. By adopting an impedance model based on the Hunt–Crossley (HC) model, the interaction in soft contact environments can be described more accurately. In the controller design, we mathematically describe the steady-state conditions of the HC-based impedance model. Then, we show how to propose a new integral terminal sliding mode manifold and the enhancement process of the traditional TDC. Finally, the superiority and effectiveness of the proposed controller are validated through comparative experiments across four different scenarios.**

Received 16 October 2025; revised 27 December 2025; accepted 5 January 2026. Date of publication 13 January 2026; date of current version 26 January 2026. This article was recommended for publication by Associate Editor C. M. Abdissa and Editor B. Wang upon evaluation of the reviewers' comments. This work was supported in part by the National Science Foundation of China under Grant 51975277 and Grant 52175097 and in part by the Fundamental Research Funds for the Central Universities-Grant under Grant NT2023011. *(Corresponding author: Yangwei Wang.)*

Zhicheng Song and Yangwei Wang are with the College of Mechanical and Electrical Engineering, Northeast Forestry University, Harbin 150040, China (e-mail: wang.yangwei@nefu.edu.cn).

Yang Wu is with the College of Mechanical and Electrical Engineering, Nanjing Forestry University, Nanjing 210037, China.

Yaoyao Wang and Jie Ling are with the College of Mechanical and Electrical Engineering, Nanjing University of Aeronautics and Astronautics, Nanjing 210016, China.

Digital Object Identifier 10.1109/TASE.2026.3653799

***Index Terms*—Cell puncture device, time-delay impedance control, Hunt–Crossley model, force/position control, adaptive, robust control.**

I. Introduction

SCHOLARS have endeavored to create diverse piezoelectric-driven cell puncture devices (PCPDs) to perform puncture operations [1], [2], [3]. When the device is in contact with the environment, it is essential to control the interaction force to ensure the safety of the device and the contact environment. Meanwhile, the position should also be well-constrained during the force control stage. Designing a controller that can accurately adjust the force and position assumes paramount significance.

To settle the interaction problem, scholars have devised a hybrid controller that surpasses pure force control by adjusting force and position. Wang and Xu [3] designed an adaptive sliding mode position controller and a proportional-integral-differential (PID) force controller to accomplish the puncture of zebrafish embryos by switching between different controllers. However, this hybrid method employs two distinct controllers, necessitating frequent switching between free space and constrained space [4], which can potentially cause system instability.

Impedance control is an effective technique for adjusting force and position simultaneously without switching controllers [5]. The control method attains the desired performance by establishing a virtual mass-spring-damping dynamic relationship that incorporates position error and contact force. It is worth pondering that if external disturbances and environment dynamics are known exactly, there is no need to design a controller to achieve interactive contact. However, in practical engineering, external disturbances are often unknown. The contact environment is usually regarded as a mass-spring-damping dynamic system that can't accurately represent the contact characteristics, especially in the micro-operation environment involving soft interaction [6].

The human body, cell, and embryo tissues typically exhibit nonlinearity, viscoelasticity, and anisotropy properties [7]. Scholars have studied linear contact models and applied them in the analysis of soft tissue mechanical characteristics and the optimization of cell puncture speed. These include the Maxwell-Wiechert [8] model, the Kelvin-Voigt [9] model, and the standard linear solid (SLS) [10] model. However, since the aforementioned models are based on linear relationships,

they cannot perfectly reproduce the complex characteristics of tissue.

The Hunt-Crossley (HC) viscoelastic model, being nonlinear, emerges as the most realistic representation for describing the mechanical behavior of soft tissue, a fact substantiated in the analysis of oocyte mechanical properties [11]. Feng et al. [6] conducted an in-depth exploration of impedance control performance based on the HC model. By integrating an integral terminal sliding mode (ITSM) manifold, an adaptive robust controller is developed for an ear surgical device, which successfully achieves force/position control on a mock membrane. Recently, Hu et al. [12] proposed a robotic micropuncture method with a preload strategy to enhance the success rate of retinal vein cannulation. First, building upon the traditional SLS model, a nonlinear viscoelastic (NV) model is introduced to characterize the dynamic relationship between preload force and tissue deformation. On this basis, an adaptive ITSM controller incorporating the NV model is adopted to achieve precise tracking control of the preloading force, and its effectiveness is successfully validated through in vitro experiments conducted on open-sky porcine eyes. Notably, the aforementioned controllers are formulated based on the system dynamics model. In micromanipulation tasks characterized by numerous unknown lumped disturbances, acquiring a dynamic model through identification proves challenging and time-consuming. Consequently, the aforementioned controllers are not conducive to practical engineering applications.

Some reinforcement learning (RL)-based trajectory control methods have been proposed, which can reduce reliance on system models through data-driven approaches. Gao et al. [13] proposed an RL-based admittance control framework for physical human-robot interaction systems with output constraints. Their approach integrates an actor-critic reinforcement learning architecture to approximate dynamic uncertainties and employs an integral barrier Lyapunov function to achieve accurate tracking while ensuring that the end-effector satisfies position constraints. Tan et al. [14] proposed a hierarchical safe RL control scheme with prescribed performance to solve the optimal safe path planning for the leader and the guaranteed tracking control for the follower in complex dynamic environments. Xue et al. [15] proposed an integrated control framework that combines prescribed performance backstepping control with RL to achieve precise trajectory tracking and optimal control for an uncrewed aerial vehicle under disturbance. To overcome the gradient dependency and slow convergence in RL-based adaptive dynamic programming (ADP), Tang et al. [16] developed a behavior-guided ADP algorithm that leverages swarm intelligence for gradient-free policy improvement and incorporates a relaxation factor to enhance convergence speed, with simulations demonstrating its effectiveness. Furthermore, RL offers a promising technical specification for variable impedance control, as demonstrated in studies such as [17], [18]. However, RL generally requires a substantial amount of training data, which is not always convenient to collect in force-tracking systems [19]. Moreover, the reliance on extensive trial-and-error to optimize policies further increases the cost of experimentation.

Time-delay control (TDC) relies solely on time-delay information for estimating dynamic characteristics and lumped disturbances within a system. This approach facilitates the construction of a control framework without relying on extensive data training or a detailed system dynamics model. Owing to these advantages, TDC has found extensive application in the motion control of intricate practical systems, including in [2], [20], and [21]. Scholars have additionally proposed force/position controllers by integrating TDC with impedance control. In the realm of upper limb rehabilitation robotics, Wu et al. [22] devised a TDC-based controller utilizing an impedance model as an ITSM manifold. For more similar studies, please refer to [23] and [24]. The aforementioned controllers employ sliding mode control (SMC) and its variants to address the well-known time-delay estimation (TDE) error. However, the application of SMC may induce chattering phenomena, which can be alleviated through the use of designed reaching law [25], super-twisting algorithm (STA) [26], [27], [28], adaptive robust terms [22], [23], and fuzzy systems [29], [30], [31], [32]. Particularly in [27], a fixed-time convergence STA (FSTA) is adopted as the reaching law to mitigate chattering and ensure the control timeliness. However, existing time-delay impedance controllers predominantly adhere to traditional TDC frameworks, where the inherent time-delay error has not been effectively addressed. To the best of the author's knowledge, few studies have sought to enhance the nature of the TDC framework and successfully apply it to the force/position control domain.

Given the aforementioned challenges, this paper designed a straightforward and efficient controller capable of simultaneous adjustment of force and position during cell puncture. This controller can achieve precise force/position control within a soft interaction environment while maintaining substantial robustness against lumped disturbances. The primary contributions of this paper are outlined below:

1) A novel adaptive robust enhanced time-delay impedance controller (ARETDIC) is proposed. The proposed ARETDIC fundamentally differs from existing time-delay impedance controllers [22], [23], [24] by introducing a tunable error term based on the previous time step's TDE, which modifies the desired error dynamics equation of the closed-loop system. This design exploits the property that consecutive TDE errors at adjacent time instants are nearly identical over small time-delay periods. Consequently, through parameter tuning, the TDE error from the previous time step can be leveraged to compensate for the current one, thereby directly and effectively enhancing control performance.

2) A new ITSM is proposed by constructing an intermediate variable, where the sliding mode variable contains the intermediate variable of the current and previous time steps, thereby endowing the intermediate variable with combined error characteristics of the present and past. Compared with the traditional ITSM [6], [22], [23], [24], the proposed sliding mode manifold has better control accuracy.

The subsequent sections of this paper are organized as follows. In Section II, the impedance model with soft contact environment is introduced based on the HC model; The proposed controller is designed in Section III; Experiments and discussions are performed in Section IV; Section V is the conclusion of this paper; Finally, the stability proof and notations table are presented in the Appendix.

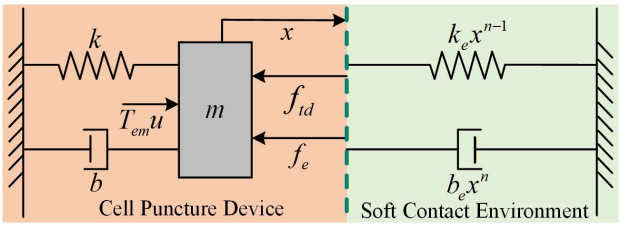

Fig. 1. Model diagram under soft contact environment.

II. Impedance Model With Soft Contact Environment

A. Soft Contact Environment

For the soft contact environment of cell puncture, a generalized dynamic model can be conceptualized as a second-order system. The specific expression of this model is expressed as follows:

$$m\ddot{x} + b\dot{x} + kx + f_{td} = T_{em}u - f_e \tag{1}$$

where m, b, k represent the mass (kg), damping (N·s/m), and stiffness (N/m) coefficients, respectively; x is the position (m); $\ddot{x}$and$\dot{x}$ are the acceleration (m/s^2) and velocity (m/s), respectively; f_{td} represents lumped disturbances (N), such as hysteresis effects and unknown model parameters, which satisfy the inequality [33]: $|f_{td}| \le \Psi_{f_{td}}$. $\Psi_{f_{td}}$ is the boundary value of lumped disturbances (N). T_{em} represents the electromechanical conversion coefficient (N/V); u represents input voltage (V); f_e represents interactive contact force (N). Fig. 1 shows a model diagram of a soft contact environment. In this model, the nonlinearity and viscoelasticity of the cell membrane are characterized by the HC model, with k_e, b_e, and n as the tissue parameters. The dynamic model of the cell puncture device is given by a second-order system (see Eq. (1)).

B. Impedance Model

To simultaneously adjust force and position, this paper utilizes a target impedance model incorporating position error and force error, as expressed in [6]:

$$m_d\ddot{e}_p + b_d\dot{e}_p + k_d e_p = -k_f e_f \tag{2}$$

where m_d, b_d and k_d are desired inertia (kg), damping (N·s/m) and stiffness (N/m) impedance parameters, respectively; k_f is an adjustable force error weight parameter; e_p and e_f are position error (m) and force error (N), respectively, and are defined as:

$$e_p = x - x_d; e_f = f_e - f_d \tag{3}$$

where x and x_d are measured position (m) and desired position (m); f_e and f_d are measured force (N) and desired force (N).

Cell tissue typically exhibits nonlinear behavior. The HC model aligns more closely with the physically intuitive characteristics of the soft interactive contact environment [34], as expressed below:

$$f_e = k_e (x - x_e)^n + b_e (x - x_e)^n \dot{x} \tag{4}$$

where x_e is the equilibrium position of the environment (m); k_e, and b_e represent the nonlinear stiffness (N/m^n), nonlinear damping (N·s/m^{n+1}) coefficients, respectively. n is a nonlinear operator. To simplify the model, we define $x_e = 0$.

C. Steady-State Analysis

To analyze the steady-state performance of the system, it is necessary to linearity the HC model. Assume that the equilibrium position corresponding to the desired force f_d is x_c. Using Taylor series at x_c, the steady-state position error e_{ps} and steady-state force error e_{fs} can be expressed as:

$$e_{ps} \approx \frac{k_f}{k_d + k_f \bar{k}_e}\left[n f_d + \bar{k}_e (x_e - x_d)\right] \tag{5}$$

$$e_{fs} \approx -\frac{k_d}{k_f} e_{ps} \approx -\frac{k_d}{k_d + k_f \bar{k}_e}\left[n f_d + \bar{k}_e (x_e - x_d)\right] \tag{6}$$

where $\bar{k}_e = n k_e (f_d/k_e)^{\frac{n-1}{n}}$.

From the steady-state response analysis of soft contact environment (see Eq. (5) and Eq. (6)), it can be observed that when $k_d \ll k_f$, the force error is significantly reduced, whereas the position error decreases when $k_d \gg k_f$. Therefore, appropriate impedance parameters can be selected according to different tasks to adjust the steady-state performance of force and position.

Note 1: Force tracking performance is particularly important in the process of cell puncture. According to Eq. (6), the zero steady-state force error of the system can be expressed as:

$$x_d = x_e + n f_d / \bar{k}_e \tag{7}$$

It can be clearly seen that if an accurate x_d can be obtained, the force trajectory tracking with zero steady-state error can be completed theoretically. However, the environment model parameters n and $\bar{k}_e$ are usually unknown, and it is challenging to obtain the actual values by identification.

III. Controller Design

A. Intermediate Variable

To design the controller independently of the parameters n and $\bar{k}_e$, an impedance error variable ξ is introduced:

$$\xi = m_d\ddot{e}_p + b_d\dot{e}_p + k_d e_p + k_f e_f \tag{8}$$

The control target is to make the impedance error variable $\lim_{t\to\infty} \xi \to 0$. Therefore, we construct:

$$B_d = b_d/m_d, K_d = k_d/m_d, K_f = k_f / m_d$$

To adjust the force and position synchronously, an intermediate variable z is defined to unify the force error and position error, which is expressed as:

$$z = \dot{e}_p + \Upsilon e_p + e_{fl} \tag{9}$$

where e_{fl} represents the force error after filtering, and satisfy:

$$\dot{e}_{fl} + \Omega e_{fl} = K_f e_f \tag{10}$$

where Υ and Ω are positive constants, and satisfy [35]:

$$\Upsilon + \Omega = B_d, \Upsilon\Omega = K_d \tag{11}$$

Substituting Eq. (9) and Eq. (10) into Eq. (8), we can obtain:

$$\bar{\xi} = \dot{z} + \Omega z \tag{12}$$

According to Eq. (12), $z = 0$ will make $\bar{\xi} = 0$, thereby the control target becomes to obtain a minimum z.

Note 2: To ensure the existence of Υ and Ω, m_d, b_d, and k_d should satisfy the following relationship:

$$b_d^2 \geq 4m_d k_d \tag{13}$$

therefore,$\Upsilon$and Ωcan expressed as:

$$\begin{cases} \Upsilon = \left(m_d^{-1} b_d \pm \sqrt{m_d^{-2} b_d^2 - 4 m_d^{-1} k_d} \right) \Big/ 2 \\ \Omega = \left(m_d^{-1} b_d \mp \sqrt{m_d^{-2} b_d^2 - 4 m_d^{-1} k_d} \right) \Big/ 2 \end{cases} \tag{14}$$

B. The Proposed Controller

According to the system dynamics model (see Eq. (1)), it can be deduced that:

$$\ddot{x} = H + \tilde{M}^{-1} u \tag{15}$$

where:

$$T_{em}^{-1} m = M;$$
$$H = -\tilde{M}^{-1} \left[T_{em}^{-1} \left(b\dot{x} + kx + f_{td} + f_e \right) + \left(M - \tilde{M} \right) \ddot{x} \right];$$

$\tilde{M}$ is a positive constant determined through experimental adjustment; H contain model parameters and nonlinear lumped disturbances, making it challenging to obtain accurate values in practical engineering. Consequently, we employ the previous time step's $H_{(t-\Delta t)}$ to estimate H, as specifically expressed: $\hat{H} \cong H_{(t-\Delta t)}$. Δt represents delayed time. When Δt is chosen as a very small value, it can be approximately considered that $H = \hat{H}$. We can further obtain:

$$\hat{H} = \ddot{x}_{(t-\Delta t)} - \tilde{M}^{-1} u_{(t-\Delta t)} \tag{16}$$

where $\ddot{x}_{(t-\Delta t)}$ is usually obtained by numerical differentiation method [27]. The accuracy of TDE depends on Δt, leading to the well-known TDE error.

To minimize the control target (intermediate variable z), we propose a new ITSM manifold. This manifold is based on the newly constructed sliding mode variable σ and is designed as follows:

$$s = \sigma + c_1 \int \left[\sigma + c_2 sig\left(\sigma\right)^{\rho} \right] dt \tag{17}$$

where $\sigma = z + z_{(t-\Delta t)}$ consists of z at the current moment and $z_{(t-\Delta t)}$ at the previous moment; $sig\left(\cdot\right)^{\rho} = |\cdot|^{\rho} \operatorname{sign}\left(\cdot\right)$, $c_1, c_2 > 0$ and $0 < \rho < 1$.

To alleviate chattering and ensure the control timeliness, we adopt the following FSTA as the reaching law to improve the local convergence, which is described as [27]:

$$\begin{cases} \dot{s} = -k_1 |s|^{1/2} \operatorname{sign}\left(s\right) - k_2 |s|^{p} \operatorname{sign}\left(s\right) + \omega, s\left(t_0\right) = s_0 \\ \dot{\omega} = -\dfrac{k_3}{2} \operatorname{sign}\left(s\right) + \varphi, \omega\left(t_0\right) = \omega_0 \end{cases} \tag{18}$$

where $k_1, k_2, k_3 > 0$ and $p > 1$. φ represent Lipschitz disturbances.

By differentiating Eq. (17) and setting it equal to Eq. (18), the following desired error dynamic equation can be obtained.

$$\begin{aligned} &\dot{\sigma} + c_1 \sigma + c_1 c_2 sig\left(\sigma\right)^{\rho} + k_1 |s|^{1/2} \operatorname{sign}\left(s\right) \\ &\quad + k_2 |s|^{p} \operatorname{sign}\left(s\right) + \frac{k_3}{2} \int \operatorname{sign}\left(s\right) = 0 \end{aligned} \tag{19}$$

For convenience in the subsequent derivation, Eq. (19) is defined as $E_{\mathrm{DED}} = 0$.

Based on the traditional TDC method, the following control law u^{TDC} can be derived to achieve the dynamics described by Eq. (19).

$$\begin{aligned} u^{\mathrm{TDC}} &= -\tilde{M}\ddot{x}_{(t-\Delta t)} + u_{(t-\Delta t)}^{\mathrm{TDC}} + \tilde{M}\left(\ddot{x}_d - \Upsilon \dot{e}_p - \dot{e}_{fl} \right. \\ &\quad - \dot{z}_{(t-\Delta t)} - c_1\sigma - c_1 c_2 sig\left(\sigma\right)^{\rho} - k_1 |s|^{1/2} \operatorname{sign}\left(s\right) \\ &\quad \left. - k_2 |s|^{p} \operatorname{sign}\left(s\right) - \frac{k_3}{2} \int \operatorname{sign}\left(s\right) \right) \\ &= -\tilde{M}\hat{H} + \tilde{M}\left(\ddot{x}_d - \Upsilon \dot{e}_p - \dot{e}_{fl} \right. \\ &\quad - \dot{z}_{(t-\Delta t)} - c_1\sigma - c_1 c_2 sig\left(\sigma\right)^{\rho} - k_1 |s|^{1/2} \operatorname{sign}\left(s\right) \\ &\quad \left. - k_2 |s|^{p} \operatorname{sign}\left(s\right) - \frac{k_3}{2} \int \operatorname{sign}\left(s\right) \right) \end{aligned} \tag{20}$$

where:

$$\begin{aligned} &\ddot{x}_d - \Upsilon \dot{e}_p - \dot{e}_{fl} - \dot{z}_{(t-\Delta t)} - c_1\sigma - c_1 c_2 sig\left(\sigma\right)^{\rho} \\ &\quad - k_1 |s|^{1/2} \operatorname{sign}\left(s\right) - k_2 |s|^{p} \operatorname{sign}\left(s\right) - \frac{k_3}{2} \int \operatorname{sign}\left(s\right) \triangleq Q \end{aligned}$$

In the traditional TDC method, $u = u^{\mathrm{TDC}}$. Therefore, substituting u into Eq. (15) yields the following traditional desired error dynamics equation for the closed-loop system.

$$E_{\mathrm{DED}} + \Xi = 0 \tag{21}$$

where TDE error is defined as: $\Xi \triangleq H - \hat{H}$, which has been proven to be bounded and satisfies: $|\Xi| \leq \Xi^{*}$. Ξ^{*} is the boundary value of the TDE error. It can be seen that the traditional TDC scheme has an unavoidable error term Ξ.

To further compensate for the TDE error, we propose a novel ETDC by using the TDE information of the previous time step. We introduce an adjustment term into the control law u_P, which is described as:

$$u_P = u - \alpha \tilde{M} \Xi_{(t-\Delta t)} \tag{22}$$

where α is a positive parameter, which needs adjustment;

$\Xi_{(t-\Delta t)}$ represents TDE information of previous time step, which is expressed as:

$$\Xi_{(t-\Delta t)} = H_{(t-\Delta t)} - H_{(t-2\Delta t)} = \hat{H} - \hat{H}_{(t-\Delta t)} \tag{23}$$

According the Eq. (22) and Eq. (23), the specific expression of the proposed control law is:

$$\begin{aligned} u_P &= -\left(1 + \alpha\right) \tilde{M}\hat{H} + \alpha \tilde{M} \hat{H}_{(t-\Delta t)} + \tilde{M} Q \\ &= -\tilde{M}\left(\hat{H} + \alpha \Xi_{(t-\Delta t)} \right) + \tilde{M} Q \end{aligned} \tag{24}$$

Therefore, the traditional desired error dynamic equation for the closed-loop system (see Eq. (21)) is enhanced as:

$$E_{\mathrm{DED}} + \Xi - \alpha \Xi_{(t-\Delta t)} = 0 \tag{25}$$

where $\Xi_{(t-\Delta t)}$ represents the TDE error from the previous time step.

Remark: Compared with the traditional TDC scheme, the proposed ETDC scheme utilizes the TDE error from the previous time step with an adjustable parameter α. According to Eq. (25), the total TDE error of the proposed ETDC scheme is $\Xi - \alpha \Xi_{(t-\Delta t)}$. Typically, to ensure control accuracy, Δt is selected to be very small, so that $\Xi_{(t-\Delta t)}$ is nearly identical to Ξ. This indicates that the current TDE error

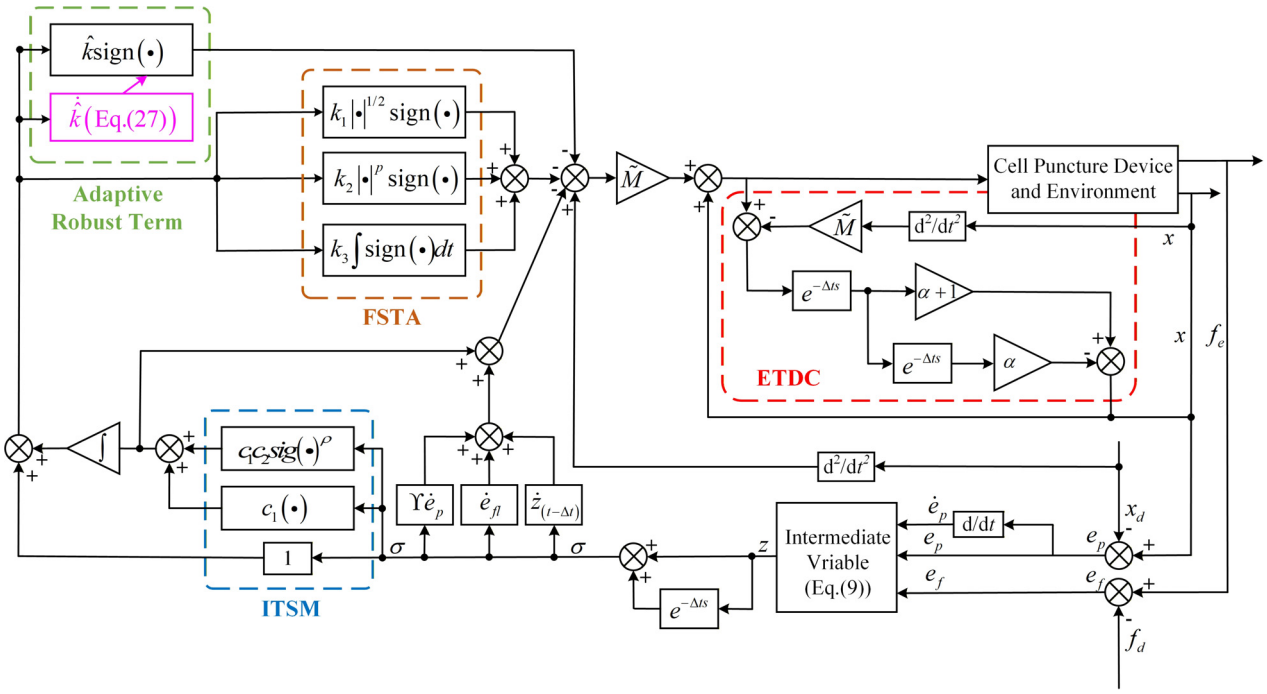

Fig. 2. Block diagram of the proposed ARETDIC.

Ξ can be reduced by introducing the previous TDE error $\Xi_{(t-\Delta t)}$. Moreover, when Δt is sufficiently small, the TDE error decreases, and the difference between Ξ and $\Xi_{(t-\Delta t)}$ becomes correspondingly small. Therefore, by adjusting α, Ξ and $\Xi_{(t-\Delta t)}$ can be made sufficiently close, thereby achieving the objective of compensating for TDE error.

Then, we propose a new adaptive switching law to design the robust component, which is displayed as follows:

$$u_{A\_P} = u_P - \tilde{M}\hat{k}\text{sign}(s) \tag{26}$$

The proposed adaptive law is as follows:

$$\dot{\hat{k}} = \begin{cases} \gamma(|s|/\mu)\,\text{sign}(|s|-\mu) & \text{if } \hat{k} > k_m \text{ or } |s| > \mu \\ 0 & \text{if } \hat{k} \le k_m \text{ and } |s| \le \mu \end{cases} \tag{27}$$

Note 3: When $|s| > \mu$, the rate increases with the distance between $|s|$ and μ, thereby ensuring that $|s|$ gradually converges towards μ. It is worth noting that $\hat{k}$ does not increase indefinitely. When $|s| \le \mu$, the adaptive gain will decrease. When both $\hat{k} \le k_m$ and $|s| \le \mu$ are satisfied simultaneously, the rate of $\hat{k}$ is constrained to zero to prevent any further reduction. From the above analysis, it is evident that $\hat{k}$ is bounded, and s can rapidly converge to μ and remain on the sliding mode manifold.

Theorem: If the sliding mode variable s enters a vicinity $\mu$by the proposed ARETDIC, s is uniformly ultimately bounded (UUB), and the boundary is shown below:

$$|s| \le \sqrt{\mu^2 + \bar{k}^*} \tag{28}$$

where $\bar{k}^*$ represents the maximum value of $\frac{\mu}{\gamma}\left(\bar{\Xi}^* - \hat{k}\right)^2$.

Detailed proof of stability is given in the Appendix. Fig. 2 presents the overall block diagram of the proposed ARETDIC, which includes Eq. (9), (22), (26), and (27), as well as all relevant control parameters.

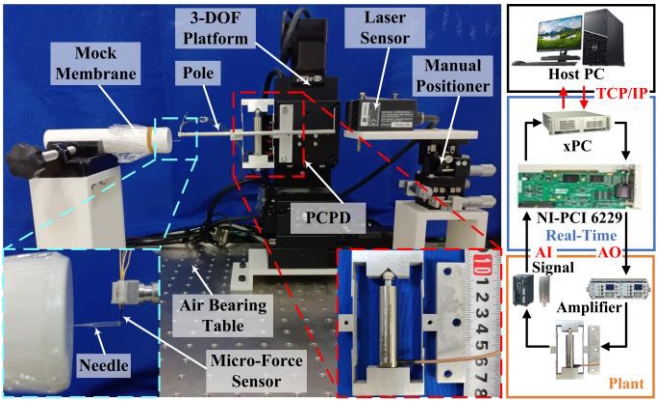

Fig. 3. Experimental system.

IV. Experiments and Discussions

A. Experimental Setup

The experimental system is illustrated in Fig. 3. To emulate the soft contact environment, we utilize soft Polyethylene as the soft mock membrane.

The interaction force and position are measured by a micro-force sensor (AE081) and a laser position sensor (LK-H022), respectively. The force and position signals are processed through a signal conditioner and amplifier and then collected by the data acquisition card's analog-to-digital channel. Control software is developed in MATLABa/Simulink on a host personal computer (PC) and transferred to the xPC system via TCP/IP. The control signal is then output through the data acquisition card's digital-to-analog channel to the voltage amplifier. To ensure high-performance control, the system's sampling frequency is set to match the upper limit of the data acquisition card, which is 10 kHz.

To verify the force tracking accuracy of the proposed ARETDIC. Three same-class benchmark controllers are selected for comparison analysis.

The first controller, designated as TDIC, is constructed based on a traditional TDC framework, where a traditional impedance model is directly adopted as the ITSM manifold, while the adaptive robust component incorporates the proposed method. The control law is presented as follows [22], [23], [24].

$$u_{\mathrm{TDIC}} = u_{(t-\Delta t)} - \tilde{M}\ddot{x}_{(t-\Delta t)} + \tilde{M}\left(\ddot{x}_d - m_d^{-1}\left[b_d\ \dot{e}_p + k_d e_p + k_f e_f\right]\right) - \tilde{M}\hat{k}\mathrm{sign}(s) \tag{29}$$

The second controller, designated as ARTDIC, is also developed within the traditional TDC framework. It adopts the traditional ITSM manifold from [6], with the sliding mode variable defined as z (see Eq. (9)). The reaching law and the adaptive robust component are identical to those in this work. The control law is presented as follows.

$$\begin{aligned} u_{\mathrm{ARTDIC}} = u_{(t-\Delta t)} &- \tilde{M}\ddot{x}_{(t-\Delta t)} + \tilde{M}\left(\ddot{x}_d - \Upsilon\dot{e}_p - \dot{e}_{fl}\right. \\ &- c_1 z - c_1 c_2 sig(z)^{\rho} - k_1 |s|^{1/2}\mathrm{sign}(s) \\ &\left. - k_2 |s|^{p}\mathrm{sign}(s) - \frac{k_3}{2}\int \mathrm{sign}(s)\right) - \tilde{M}\hat{k}\mathrm{sign}(s) \end{aligned} \tag{30}$$

The third controller, designated as ARETDIC_I, is constructed based on the proposed ETDC framework. It retains the traditional ITSM manifold from [6], while employing the same reaching law and adaptive robust component as those introduced in this paper. The control law is given as follows.

$$\begin{aligned} u_{\mathrm{ARETDIC\_I}} = &-(1+\alpha)\tilde{M}\hat{H} + \alpha\tilde{M}\hat{H}_{(t-\Delta t)} \\ &+ \tilde{M}\left(\ddot{x}_d - \Upsilon\dot{e}_p - \dot{e}_{fl}\right. \\ &- c_1 z - c_1 c_2 sig(z)^{\rho} - k_1 |s|^{1/2}\mathrm{sign}(s) \\ &\left. - k_2 |s|^{p}\mathrm{sign}(s) - \frac{k_3}{2}\int \mathrm{sign}(s)\right) - \tilde{M}\hat{k}\mathrm{sign}(s) \end{aligned} \tag{31}$$

B. Influence of Impedance Parameters

Firstly, we studied the influence of impedance parameters on the force and position steady-state performance of the proposed ARETDIC. The desired force and position follow step trajectories with amplitudes of 0.5mN and 60μm, respectively. The impedance parameters are selected as: $m_d = 0.0015$, $b_d = 300, k_d = 500$. For fairness, m_d, b_d,and k_d remain unchanged, and only k_f changes from 1 to 10000 to study the influence of k_f on steady-state performance. The force and position tracking results of the proposed ARETDIC are shown in Fig. 4.

For $k_f = 1$, the steady-state force is 0.265mN, and the corresponding position is 65.06μm. For $k_f = 10000$, the steady-state force increases to 0.507mN, while the steady-state position reaches 96.50μm. As k_f increases, the force tracking performance significantly improves, whereas the position tracking performance noticeably deteriorates.

To quantify analysis, we employ the root-mean-square error (RMSE) as the evaluation indicator. As k_f increases from 1 to 10000, the steady-state RMSE value for force significantly decreases from 0.233mN to 0.00608mN. Conversely, the steady-state RMSE value for position increases from 6.029μm to 37.019μm. The experimental results validate that the steady-state performance aligns with the analytical outcomes from Eq. (5) and Eq. (6). Notably, force performance exhibits higher sensitivity to changes in k_f, while position error persists for $k_f \neq 0$.

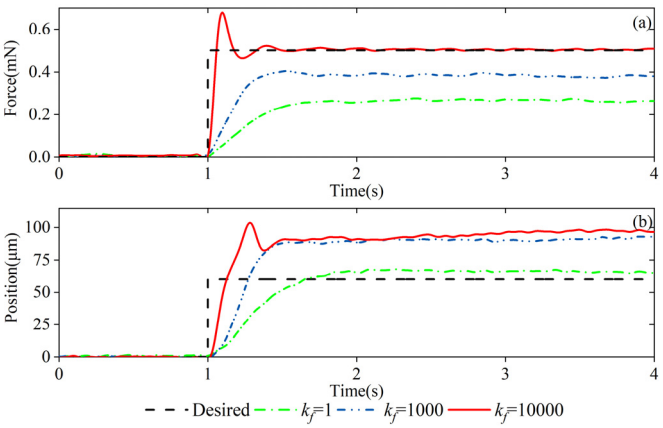

Fig. 4. Tracking results of the proposed ARETDIC for the step trajectory under different k_f.

C. Performance Comparison of Force Tracking

The parameters of the proposed ARETDIC are adjusted by the trial-and-error method. For a detailed explanation of the TDC parameters adjustment process, please refer to Note 4.

Note 4: To achieve satisfactory control performance, the parameter tuning process adheres to the following guidelines:

(1): The initial values of impedance parameters m_d, b_d, and k_d must be predetermined, and thus Υ is also known.

(2): Set $c_1 = c_2 = 1$ and $k_1 = k_2 = k_3 = 0$. $\tilde{\mathrm{M}}$ is initialized at a very small value and gradually increased until degradation in control performance is observed. An adjustment process similar to $\tilde{\mathrm{M}}$ can be used to determine c_1 and c_2.

(3): Maintain $k_1 = k_2 = k_3 = 0$. Gradually decrease ρ from 1 to the appropriate value, while monitoring both the control error and chattering.

(4): Maintain $k_2 = k_3 = 0$. Tune $k_1$by increasing it from 0 to the appropriate value, while checking the control error and chattering. k_2 and k_3 can be determined using a similar tuning procedure to k_1.

(5): An appropriate value for k_{m} should be selected based on the observed control performance. Tune γ by increasing it from 0 to the appropriate value and tune μ by decreasing it from a large value to a small value, while monitoring both the control error and chattering.

(6): k_d defines the static relationship between force and position. As the core parameter of the impedance model, it should be determined first. Maintain m_d and b_d unchanged. Tune k_d by increasing or decreasing it to the appropriate value, while checking the control error and chattering. Then, maintain m_d and k_d unchanged. Tune b_d by increasing or decreasing its value until it is appropriate, while checking system oscillation. Finally,

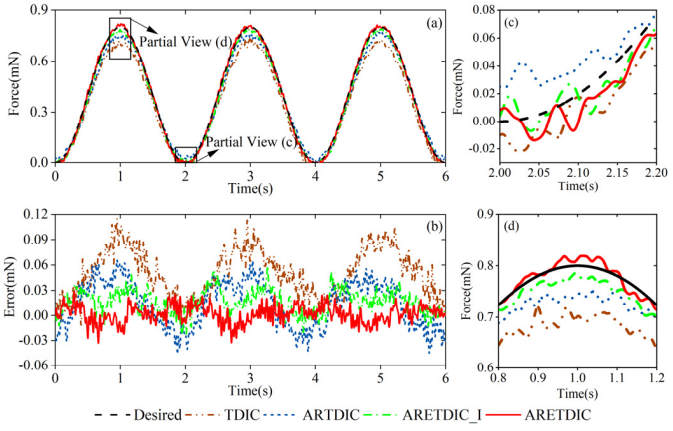

Fig. 5. Force tracking results of the cosine trajectory for the different controllers. (a). Trajectory tracking. (b). Trajectory errors. (c). Partial view of the force trough. (d). Partial view of the force peak.

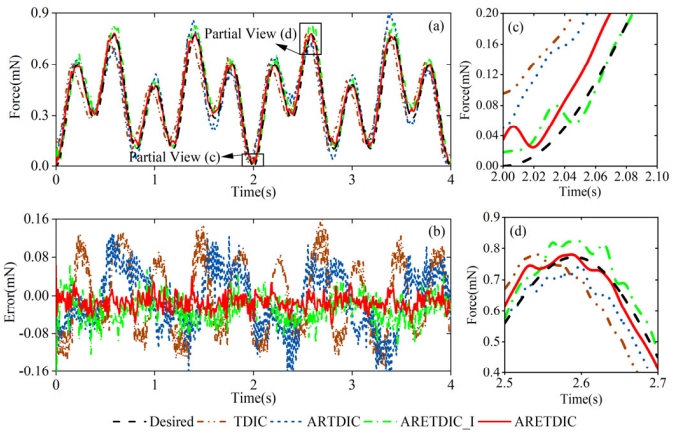

Fig. 6. Force tracking results of the compound frequency trajectory for the different controllers. (a). Trajectory tracking. (b). Tracking errors. (c). Partial view of the force trough. (d). Partial view of the force peak.

with b and k held constant, tune m by increasing or decreasing it to the appropriate value, while checking the dynamic response.

(7): Tune α by Increasing It From 0 to the Appropriate Value, While Checking the Control Error and Chattering If the control performance fails to meet the desired level, the aforementioned steps should be repeated accordingly.

The impedance parameters are selected as: $m_d = 0.0015$, $b_d = 300, k_d = 500, k_f = 10000$. The control parameters are as: $\Delta t = 0.0001$, $\tilde{M} = 0.105 \times 10^{-5}$, $\alpha = 0.3, c_1 = 1.6, c_2 = 1.7$, $\rho = 0.4, p = 1.3, k_1 = 30, k_2 = 2.6, k_3 = 54$, $\gamma = 0.06$, $\mu = 0.005$, $k_m = 3.5$. To ensure fairness, the parameters of ARETDIC_I are identical to those of ARETDIC, differing only in the ITSM manifold. The control parameters of ARTDIC don't include the parameter α, while all other parameters are consistent with those of ARETDIC_I. Since the ITSM manifold of TDIC is defined by impedance parameters, all its parameters are identical to those of the corresponding positions in ARETDIC. Notably, the robustness components of all benchmark controllers align with Eq. (27). Fig. 5 and Fig. 6 show the tracking results of all controllers for different force trajectories. The performance comparisons are listed in Table I.

TABLE I
PERFORMANCE COMPARISONS OF FORCE TRAJECTORIES

Controller	Indicators (mN)	Cosine	Compound Frequency
TDIC	e_{RMSE}	0.0578	0.0743
	e_{MAX}	0.1153	0.1438
ARTDIC	e_{RMSE}	0.0310	0.0576
	e_{MAX}	0.0748	0.1462
ARETDIC_I	e_{RMSE}	0.0219	0.0359
	e_{MAX}	0.0592	0.1301
ARETDIC	e_{RMSE}	0.0105	0.0201
	e_{MAX}	0.0331	0.0864

In Fig. 5, all controllers successfully track the cosine trajectory. Notably, the proposed ARETDIC demonstrates superior force tracking accuracy. In contrast, the TDIC and ARTDIC exhibit lower control accuracy due to their reliance on traditional TDC, which introduces unavoidable time-delay error. The proposed ARETDIC_I and ARETDIC use the time-delay information of the previous time step to further compensate for the time-delay error, leading to a significant reduction in error (see Fig. 5(b)). As observed in Fig. 5(c, d), during abrupt changes at the force troughs and peaks, the proposed ARETDIC_I and ARETDIC exhibit superior transient performance compared to the other two controllers. Notably, during the passage through the force peak, the proposed ARETDIC follows the desired trajectory more closely without exhibiting either overshoot or undershoot. In contrast, due to differences in the design of their sliding manifolds, the proposed ARETDIC_I shows a slight undershoot (see Fig. 5(d)). These results further confirm the advantage of the proposed ITSM manifold over the traditional ITSM manifold.

Compared to TDIC, the proposed ARETDIC achieves reductions of 81.83% in e_{RMSE} and 71.29% in e_{MAX}. Relative to ARETDIC_I, ARETDIC further reduces e_{RMSE} and e_{MAX} error by 52.05% and 44.09%, respectively (see Table. I). The above experimental results demonstrate that the proposed ARETDIC can compensate for the time-delay error and accurately track the desired force trajectory, which can significantly improve the control accuracy of the existing time-delay impedance controller.

For the compound frequency trajectory (see Fig. 6), the tracking performance of four controllers shows a decreasing trend due to the trajectory's complexity. Facing frequent variations between force troughs and peaks, the proposed ARETDIC_I and ARETDIC still maintain the best transient response (see Fig. 6(c, d)). As shown in Fig. 6(d), benefiting from the proposed ITSM manifold, the proposed ARETDIC continues to exhibit neither overshoot nor undershoot and still retains the smallest tracking error among the four controllers. Specifically, compared to TDIC, the proposed ARETDIC achieves reductions in e_{RMSE} and e_{MAX} by 72.95% and 39.92%, respectively. In comparison with ARETDIC_I, the proposed ARETDIC yields decreases in e_{RMSE} and e_{MAX} of 44.01% and 33.59%, respectively (see Table. I). The exper-

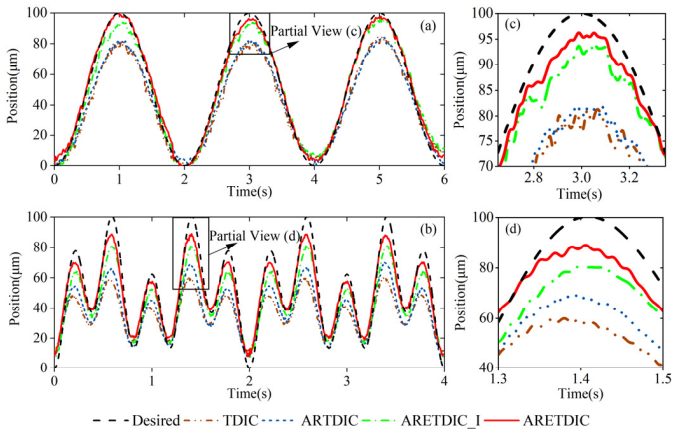

Fig. 7. Position tracking results of the different trajectories for the different controllers. (a). Cosine trajectory. (b). Compound frequency trajectory. (c). Partial view of the position peak in the cosine trajectory (d). Partial view of the position peak in the compound frequency trajectory.

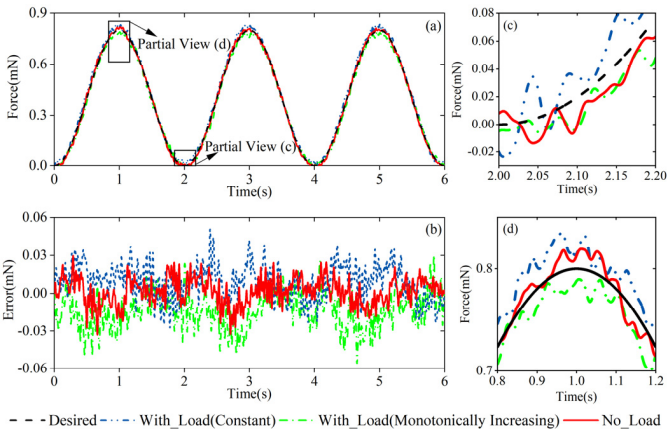

Fig. 8. Force tracking results under no load, monotonically increasing load, and constant load. (a). Trajectory tracking. (b). Tracking errors. (c). Partial view of the force trough. (d). Partial view of the force peak.

imental results confirm the proposed ARETDIC's ability to accurately track the desired force across different trajectories under soft interaction.

During force control, the measurement results for position trajectory tracking are presented in Fig. 7. Although the desired position follows the standard trajectory, a deviation is observed in the measured position. This indicates the presence of nonlinearity, viscoelasticity, and anisotropy in the soft membrane contact—characteristics that differ from those of the environment described in [36]. This discrepancy also explains the degradation observed in the position transient response of the four controllers. As shown in Fig. 7(c, d), all controllers exhibit undershoot in their tracking performance when passing the position peak. Nevertheless, the proposed ARETDIC still demonstrates the best position-constraining capability. However, with the change from a cosine signal to a complex frequency signal, the trajectory complexity and contact frequency increase, and the position depth decreases accordingly. Nonetheless, even under such circumstances, the proposed ARETDIC demonstrates enhanced positional constraint capabilities along the contact direction while achieving precise force tracking.

D. Robustness of the Proposed Controller

The weight of the cell puncture device is 0.1 kg. The desired force follows a cosine trajectory. Then, a constant load of 0.022 kg is added to the puncture rod (about 20% of the total weight). Subsequently, a low-density sponge with an initial weight of 0.005 kg is added to the puncture rod. A peristaltic pump with a constant flow rate of 1.865 ml/s injects water continuously into the sponge. The control time is set to 6s, and the monotonically increasing load is guaranteed to increase from 0.005 kg to 0.011 kg. The corresponding force tracking results are shown in Fig. 8. The performance comparisons are listed in Table II.

As shown in Fig. 8(b), the overall error is the smallest under no-load conditions. From Fig. 8(c, d), it can be observed that the transient response during force troughs and peaks degrades slightly under loading compared to that under no-load conditions. Specifically, the e_{RMSE} and e_{MAX} under no-load conditions are reduced by 46.15% and 40.68%, respectively, compared to those under constant loading, and by 34.38% and 34.71%, respectively, compared to those under monotonically increasing loading (see Table II). Experimental results demonstrate that the proposed ARETDIC maintains superior force control accuracy even under lumped disturbances. Moreover, its control performance under load significantly surpasses that of the other three controllers under no-load, further confirming the proposed ARETDIC's advantages in control accuracy and robustness.

TABLE II
PERFORMANCE COMPARISONS OF ROBUSTNESS

Indicators(mN)	No Load	Monotonically Increasing Load	Constant Load
e_{RMSE}	0.0105	0.0160	0.0195
e_{MAX}	0.0331	0.0507	0.0558

E. Cell Puncture Experiment

The experimental system (See Fig. 11) involves a zebrafish embryo as the target specimen, with the procedure segmented into three main stages: penetration, injection, and retraction [3]. Before the actual work, the tip of the puncture needle is in critical contact with the zebrafish embryo. Then, a quadratic curve is used as the desired force trajectory to guide the puncture needle into the zebrafish embryo. At this stage, accurate force tracking is key to ensuring successful puncture. A small contact force will cause the injection needle to fail to penetrate the embryo yolk, while a large contact force will damage the embryo yolk. Moreover, it is also necessary to impose position constraints to ensure the stability of the interaction. When the embryo yolk is penetrated and the contact is stable, the system enters the position control stage. First, ensuring that the position remains unchanged, the nutrients are injected into the yolk, and then the injection needle is returned to its initial position according to the desired positional trajectory. The whole puncture process is then complete. Notably, the

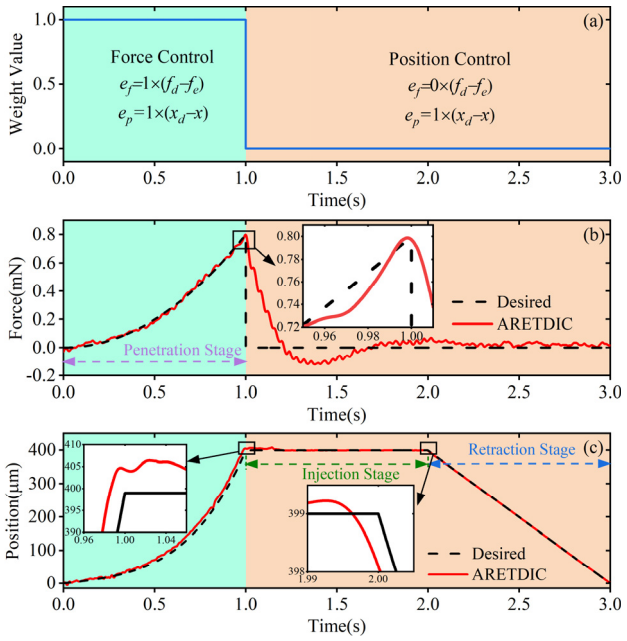

Fig. 9. Experimental results of cell puncture. (a) Weight value between position and force. (b) Force trajectory tracking. (c) Position trajectory tracking.

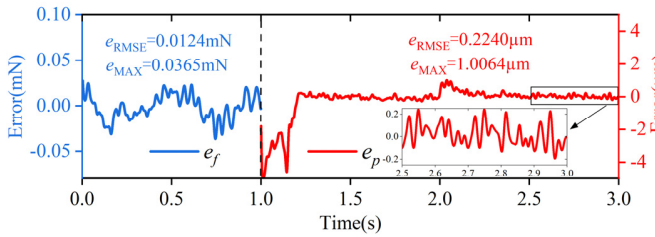

Fig. 10. Force and position errors during the cell puncture.

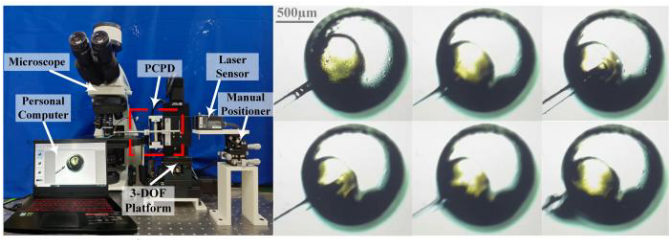

Fig. 11. Cell puncture system and image sequence.

proposed ARETDIC can be converted into a position controller by manipulating the impedance model (See Eq. (2)) and minimizing the force error to zero, thereby ensuring precise force/position control for cell puncture. Because of the distinct materials of soft Polyethylene and the Zebrafish tissue, the impedance parameters are readjusted to $m_d = 0.0018$, $b_d = 240$, $k_d = 106$, $k_f = 10000$ by trial-and-error method. The experimental results of cell puncture are shown in Fig. 9 and Fig. 10.

As illustrated in Fig. 9, the proposed ARETDIC demonstrates precise tracking ability of the desired force trajectory. However, there is a significant error between the measured and the desired position. During the force control stage, it is impossible to reach the desired position, which is consistent with the analysis of Eq. (5) and Eq. (6). Nonetheless, the proposed ARETDIC still effectively constrains the position of the cell puncture device. During the position tracking stage, the proposed ARETDIC accurately follows the desired position trajectory. Upon transitioning between force and position control, an increase in position error occurs momentarily, followed by gradual error convergence (see Fig. 10). Due to abrupt parameter changes, this transient response is normal and can be effectively mitigated by incorporating a smoothing algorithm in subsequent design. Importantly, because the controller remains unchanged, stability is ensured according to the proposed Theorem. Fig. 10 illustrates the force and position errors during puncture. For force control, e_{RMSE} and e_{MAX} are 0.0124mN and 0.0365mN, respectively. For position control, according to the data analysis from 1.5s to 3s, e_{RMSE} and e_{MAX} are 0.2240μm and 1.0064μm, respectively. These findings demonstrate that the proposed ARETDIC achieves accurate force/position control, facilitating successful cell puncture through simultaneous adjustment of force and position. The microscopically observed image sequence is depicted in Fig. 11.

V. Conclusion

This paper proposes a novel ARETDIC for a PCPD, aiming to fulfill force/position control requirements of cell puncture within a soft contact environment. The investigation explores the influence of the target impedance model on steady-state position and force performance within a soft contact environment, employing the HC model. Introducing a new ITSM manifold by constructing an intermediate variable enhances the system error dynamics equation. Omitting complex system modeling, the dynamic characteristics of the system are estimated by TDE technology. Notably, the well-known time-delay error is compensated by superimposing the time-delay information from the previous moment, thereby improving the control accuracy of the traditional TDC. Furthermore, a new adaptive robust term is proposed to enhance controller robustness. The stability of the proposed ARETDIC is proven using the Lyapunov theory. The influence of impedance parameters on steady-state force error and steady-state position error is evaluated by experiments. Comparisons with the other three benchmark controllers validate its force tracking performance, position constraint capability, and robustness, with ARETDIC exhibiting superior control performance. The effectiveness of the proposed ARETDIC is confirmed through successful application in cell puncture with zebrafish embryos, affirming its practicability.

The proposed control framework demonstrates significant potential for extension to other precision robotic systems that often face challenges in obtaining accurate dynamic models. This includes surgical robots, micro-assembly robots, and haptic devices that interact with uncertain environments. By not relying on explicit system models, this method offers a practical and robust solution for engineering tasks characterized by nonlinearity and uncertainty.

It is worth noting that this paper adopts an intuitive approach, aligned with the definition of robustness, to analyze the controller's robustness. Although the experimental results

confirm the robustness of the proposed ARETDIC, quantitative analysis of this robustness remains absent due to the inherent complexity and strong nonlinearity of piezoelectric systems. Future research will focus on developing quantitative robustness evaluation methods, including addressing the issue through frequency-domain analysis of nonlinear systems.

APPENDIX A

To prove the stability of the closed-loop system, we choose the following Lyapunov function:

$$V = \frac{1}{2}s^2 + \frac{1}{2}\frac{\mu}{\gamma}\left(\bar{\Xi}^* - \hat{k}\right)^2 \tag{32}$$

where $\bar{\Xi}^*$ represent upper boundary of $\left\|\Xi - \alpha\Xi_{(t-\Delta t)}\right\|$.

The derivation of Eq. (32) can be obtained:

$$\begin{aligned}\dot{V} &= s\dot{s} + \frac{\mu}{\gamma}\left(\bar{\Xi}^* - \hat{k}\right)\dot{\hat{k}} \\ &= s\left(\ddot{x} - \ddot{x}_d + \Upsilon\dot{e}_p + \dot{e}_{fl} + \dot{z}_{(t-\Delta t)} + c_1\sigma + c_1c_2\text{sign}\,(\sigma)^\beta\right) \\ &\quad - \frac{\mu}{\gamma}\left(\bar{\Xi}^* - \hat{k}\right)\dot{\hat{k}} \\ &= s\left(H + \tilde{M}^{-1}u - \ddot{x}_d + \Upsilon\dot{e}_p + \dot{e}_{fl} + \dot{z}_{(t-\Delta t)} + c_1\,\sigma\right. \\ &\quad \left. + c_1c_2\text{sign}\,(\sigma)^\beta\right) \\ &\quad - \frac{\mu}{\gamma}\left(\bar{\Xi}^* - \hat{k}\right)\dot{\hat{k}}\end{aligned} \tag{33}$$

Substituting u_{A_P} into $u$in Eq. (33), the upper bound of $\dot{V}$ can be expressed as:

$$\begin{aligned}\dot{V} &= s\dot{s} + \frac{\mu}{\gamma}\left(\bar{\Xi}^* - \hat{k}\right)\dot{\hat{k}} \\ &= s\left(\Xi - \alpha\Xi_{(t-\Delta t)} - k_1\,|s|^{1/2}\,\text{sign}\,(s) - k_2\,|s|^p\,\text{sign}\,(s)\right. \\ &\quad \left. - \frac{k_3}{2}\int \text{sign}\,(s) - \hat{k}\text{sign}\,(s)\right) - \frac{\mu}{\gamma}\left(\bar{\Xi}^* - \hat{k}\right)\dot{\hat{k}} \\ &= -k_1\,|s|^{3/2} - k_2\,|s|^{p+1} - \frac{k_3}{2}\int |s| \\ &\quad + s\left(\Xi - \alpha\Xi_{(t-\Delta t)} - \hat{k}\text{sign}\,(s)\right) - \frac{\mu}{\gamma}\left(\bar{\Xi}^* - \hat{k}\right)\dot{\hat{k}} \\ &\le -k_1\,|s|^{3/2} - k_2\,|s|^{p+1} - \frac{k_3}{2} \\ &\quad \int |s| + \left(\bar{\Xi}^* - \hat{k}\right)|s| - \frac{\mu}{\gamma}\left(\bar{\Xi}^* - \hat{k}\right)\dot{\hat{k}} \\ &= -k_1\,|s|^{3/2} - k_2\,|s|^{p+1} - \frac{k_3}{2} \\ &\quad \int |s| + \left(\bar{\Xi}^* - \hat{k}\right)\left(|s| - (\mu/\gamma)\,\dot{\hat{k}}\right)\end{aligned} \tag{34}$$

According to the proposed adaptive switching law, the following cases are considered.

For $|s| > \mu$, Eq. (27) ensures that $\dot{V}$ is negative definite and satisfies inequality:

$$\dot{V} \le -k_1\,|s|^{3/2} - k_2\,|s|^{p+1} - \frac{k_3}{2}\int |s| \tag{35}$$

where k_1, k_2, k_3 are positive parameters.

For $|s| \le \mu$, Eq. (27) does not ensure that $\dot{V}$ is negative and satisfies inequality:

$$\begin{cases}\dot{V} \le -k_1\,|s|^{3/2} - k_2\,|s|^{p+1} - \dfrac{k_3}{2}\displaystyle\int |s| + 2\left(\bar{\Xi}^* - \hat{k}\right)|s| \\ \dot{V} \le -k_1\,|s|^{3/2} - k_2\,|s|^{p+1} - \dfrac{k_3}{2}\displaystyle\int |s| + \left(\bar{\Xi}^* - \hat{k}\right)|s|\end{cases} \tag{36}$$

Based on V, the boundary of $|s|$for $|s| \le \mu$is obtained:

$$\frac{1}{2}s^2 \le V \le \frac{1}{2}s^2 + \frac{1}{2}\frac{\mu}{\gamma}\left(\bar{\Xi}^* - \hat{k}\right)^2 \tag{37}$$

When $|s| > \mu$, Vdecreases until $|s| \le \mu$, Vexists an upper bound for $|s| \le \mu$.

$$V \le \frac{1}{2}\mu^2 + \frac{1}{2}\frac{\mu}{\gamma}\left(\bar{\Xi}^* - \hat{k}\right) \tag{38}$$

There exists a $\bar{k}^*$such that:

$$V \le 0.5\mu^2 + 0.5\bar{k}^* \tag{39}$$

where $\bar{k}^*$ is the maximum value of $\frac{\mu}{\gamma}\left(\bar{\Xi}^* - \hat{k}\right)^2$.

According to the Eq. (38) and Eq. (39), we can obtain the upper bound of s for $|s| \le \mu$:

$$|s| \le \sqrt{\mu^2 + \bar{k}^*} \tag{40}$$

it can be seen that the proposed ARETDIC is UUB.

To sum up, the proof is completed.

APPENDIX B

NOTATIONS

Symbol	Description
m	Mass.
e_{fl}	Force Error After Filtering.
b	Damping.
x	Measured Position.
k	Stiffness.
x_d	Desired Position.
$\ddot{x}$	Acceleration.
f_d	Desired Force.
$\dot{x}$	Velocity.
x_e	Equilibrium Position.
$\mathrm{f_{td}}$	Umped Disturbances.
e_{ps}	Steady-State Position Error.
$\Psi_{f_{id}}$	Lumped Disturbances' Boundary Value.
e_{fs}	Steady-State Force Error.
$\mathrm{T_{em}}$	Electromechanical Conversion Coefficient.
z	Intermediate Variable.
u	Input Voltage.
s	Sliding Mode Manifold.
$\mathrm{f_e}$	Contact/Measured Force.
c_1, c_2, ρ	Sliding Mode Manifold Parameters.
k_e	Nonlinear Stiffness Coefficient.
σ	Sliding Mode Variable.
b_e	Nonlinear Damping Coefficient.
k_1, k_2, k_3, p	Reaching Law Parameters.
n	Nonlinear Operator.
Ξ	TDE Error.
m_d	Desired Inertia.
Ξ^*	TDE Error's Boundary Value.
b_d	Desired Damping.
$\tilde{M}$	TDE Control Parameter.
k_d	Desired Stiffness.
α	TDE Adjustment Parameter.
k_f	Force Error Weight Parameter.
Δt	Delayed Time.

e_p	Position Error.
$\hat{k}$	Adaptive Gain.
e_f	Force Error.
γ, μ, k_m	Adaptive Gain Parameters.

REFERENCES

[1] X. Gao et al., "A compact 2-DOF cross-scale piezoelectric robotic manipulator with adjustable force for biological delicate puncture," *IEEE Trans. Robot.*, vol. 40, pp. 4561–4577, 2024.

[2] M. Xie, S. Yu, H. Lin, J. Ma, and H. Wu, "Improved sliding mode control with time delay estimation for motion tracking of cell puncture mechanism," *IEEE Trans. Circuits Syst. I, Reg. Papers*, vol. 67, no. 9, pp. 3199–3210, Sep. 2020.

[3] G. Wang and Q. Xu, "Design and precision position/force control of a piezo-driven microinjection system," *IEEE/ASME Trans. Mechatronics*, vol. 22, no. 4, pp. 1744–1754, Aug. 2017.

[4] T. Kim, S. Yoo, T. Seo, H. S. Kim, and J. Kim, "Design and force-tracking impedance control of 2-DOF wall-cleaning manipulator via disturbance observer," *IEEE/ASME Trans. Mechatronics*, vol. 25, no. 3, pp. 1487–1498, Jun. 2020.

[5] Q. Xu, "Robust impedance control of a compliant microgripper for high-speed position/force regulation," *IEEE Trans. Ind. Electron.*, vol. 62, no. 2, pp. 1201–1209, Feb. 2015.

[6] Z. Feng, W. Liang, J. Ling, X. Xiao, K. K. Tan, and T. H. Lee, "Adaptive robust impedance control for an ear surgical device with soft interaction," *IEEE/ASME Trans. Mechatronics*, vol. 27, no. 3, pp. 1784–1795, Jun. 2022.

[7] A. Pappalardo, A. Albakri, C. Liu, L. Bascetta, E. De Momi, and P. Poignet, "Hunt–Crossley model based force control for minimally invasive robotic surgery," *Biomed. Signal Process. Control*, vol. 29, pp. 31–43, Aug. 2016.

[8] A. Hajiyavand, M. Saadat, A. Abena, F. Sadak, and X. Sun, "Effect of injection speed on oocyte deformation in ICSI," *Micromachines*, vol. 10, no. 4, p. 226, Mar. 2019.

[9] F. Wang and C. Wang, "Blow-up and global existence analysis for the viscoelastic wave equation with a frictional and a kelvin-voigt damping," *Adv. Math. Phys.*, vol. 2018, pp. 1–10, May 2018.

[10] S. Kang, X. Yang, Y. Li, H. Wu, and T. Li, "A fractional viscoelastic mechanical model for speed optimization of robotic cell microinjection," *IEEE/ASME Trans. Mechatronics*, vol. 29, no. 6, pp. 4514–4525, Dec. 2024.

[11] J. Kim and J. Kim, "Viscoelastic characterization of mouse zona pellucida," *IEEE Trans. Biomed. Eng.*, vol. 60, no. 2, pp. 569–575, Feb. 2013.

[12] B. Hu et al., "Robotic micropuncture with preload strategy for retinal vein cannulation," *IEEE/ASME Trans. Mechatronics*, early access, Aug. 11, 2025, doi: 10.1109/TMECH.2025.3593419.

[13] H. Gao, Y. Yang, J. Liu, and C. Sun, "Reinforcement learning-based admittance control for physical human–robot interaction with output constraints," *IEEE Trans. Autom. Sci. Eng.*, vol. 22, pp. 16334–16345, 2025.

[14] J. Tan, S. Xue, H. Li, Z. Guo, H. Cao, and B. Chen, "Hierarchical safe reinforcement learning control for leader-follower systems with prescribed performance," *IEEE Trans. Autom. Sci. Eng.*, vol. 22, pp. 19568–19581, 2025.

[15] S. Xue, J. Tan, T. Niu, K. Qu, H. Cao, and B. Chen, "Prescribed performance optimized control of UAV with robust approximate dynamic programming under disturbance," *IEEE Trans. Ind. Electron.*, early access, Oct. 23, 2025, doi: 10.1109/TIE.2025.3605451.

[16] G. Tang, D. Wang, A. Liu, and J. Qiao, "Adjustable behavior-guided adaptive dynamic programming for neural learning control," *Neurocomputing*, vol. 636, Jul. 2025, Art. no. 129986.

[17] Y. Li, L. Zheng, Y. Wang, E. Dong, and S. Zhang, "Impedance learning-based adaptive force tracking for robot on unknown terrains," *IEEE Trans. Robot.*, vol. 41, pp. 1404–1420, 2025.

[18] Y. Li, Y. Wang, Z. Li, L. Yingxiang, J. Chai, and E. Dong, "Deep reinforcement learning-based variable impedance control for grinding workpieces with complex geometry," *Robotic Intell. Autom.*, vol. 45, no. 1, pp. 159–172, Feb. 2025.

[19] J. Duan, Y. Gan, M. Chen, and X. Dai, "Adaptive variable impedance control for dynamic contact force tracking in uncertain environment," *Robot. Auto. Syst.*, vol. 102, pp. 54–65, Apr. 2018.

[20] M. Pi, "Adaptive time-delay attitude control of jumping robots based on voltage control model," *IEEE Robot. Autom. Lett.*, vol. 9, no. 5, pp. 4503–4510, May 2024.

[21] J. Yang, Y. Wang, T. Wang, Z. Hu, X. Yang, and J. J. Rodriguez-Andina, "Time-delay sliding mode control for trajectory tracking of robot manipulators," *IEEE Trans. Ind. Electron.*, vol. 71, no. 10, pp. 13083–13091, Oct. 2024.

[22] Q. Wu, D. Xu, B. Chen, and H. Wu, "Integral fuzzy sliding mode impedance control of an upper extremity rehabilitation robot using time delay estimation," *IEEE Access*, vol. 7, pp. 156513–156525, 2019.

[23] M. M. Rayguru, M. R. Elara, B. F. Gomez, and B. Ramalingam, "A time delay estimation based adaptive sliding mode strategy for hybrid impedance control," *IEEE Access*, vol. 8, pp. 155352–155361, 2020.

[24] Z. Wu, Y. Chen, Y. Geng, X. Wang, and B. Xuan, "Model-free robust adaptive integral sliding mode impedance control of knee–ankle–toe active transfemoral prosthesis," *Int. J. Med. Robot. Comput. Assist. Surgery*, vol. 18, no. 3, pp. e237–8, Jun. 2022.

[25] S. Yu, H. Wu, M. Xie, H. Lin, and J. Ma, "Precise robust motion control of cell puncture mechanism driven by piezoelectric actuators with fractional-order nonsingular terminal sliding mode control," *Bio-Design Manuf.*, vol. 3, no. 4, pp. 410–426, Jul. 2020.

[26] M. Zhou, H. Su, Y. Feng, K. Wei, W. Xu, and J. Cheng, "Super-twisting algorithm-based fractional-order sliding-mode control of nonlinear systems with mismatched uncertainties," *IEEE Trans. Ind. Electron.*, vol. 71, no. 8, pp. 9510–9519, Aug. 2024.

[27] Z. Song et al., "Time-delay control scheme with adaptive fixed-time convergent super-twisting fractional-order nonsingular terminal sliding mode for piezoelectric displacement amplifier," *ISA Trans.*, vol. 146, pp. 99–113, Mar. 2024.

[28] A. T. Demora and C. M. Abdissa, "Neural network-based lower limb prostheses control using super twisting sliding mode control," *IEEE Access*, vol. 13, pp. 24929–24953, 2025.

[29] D. F. Assefa, E. A. Gedefaw, C. M. Abdissa, and L. N. Lemma, "Adaptive neuro-fuzzy inference system-based sliding mode control in the presence of external disturbances and parameter variation for quadcopter UAV," *Eng. Rep.*, vol. 7, no. 10, pp. e7041–7, Sep. 2025.

[30] T. H. Gebrecherkos, A. G. Berhe, S. Gurusamy, and C. M. Abdissa, "Fuzzy sliding mode control for dynamic walking assistance in lower limb exoskeletons," *IEEE Access*, vol. 13, pp. 161235–161249, 2025.

[31] A. G. Adane and C. M. Abdissa, "Adaptive fuzzy sliding mode controller of three link robot arm manipulator," *IEEE Access*, vol. 13, pp. 158222–158236, 2025.

[32] G. M. Eneyew, W. A. Asfaw, and C. M. Abdissa, "Optimized backstepping fuzzy sliding mode controller for trajectory tracking of mobile manipulator," *Eng. Rep.*, vol. 7, no. 7, pp. e7026–9, Jul. 2025.

[33] A. Safa, R. Y. Abdolmalaki, and H. C. Nejad, "Precise position tracking control with an improved transient performance for a linear piezoelectric ceramic motor," *IEEE Trans. Ind. Electron.*, vol. 66, no. 4, pp. 3008–3018, Apr. 2019.

[34] C. Ng, W. Liang, C. W. Gan, H. Y. Lim, and K. K. Tan, "Optimization of the penetrative path during grommet insertion in a robotic ear surgery," *Mechatronics*, vol. 60, pp. 1–14, Jun. 2019.

[35] Y. Li, S. Sam Ge, and C. Yang, "Learning impedance control for physical robot–environment interaction," *Int. J. Control*, vol. 85, no. 2, pp. 182–193, Feb. 2012.

[36] Q. Xu, "Precision position/force interaction control of a piezoelectric multimorph microgripper for microassembly," *IEEE Trans. Autom. Sci. Eng.*, vol. 10, no. 3, pp. 503–514, Jul. 2013.